Local Xenon-Protein Interaction Produces Global Conformational Change and Allosteric Inhibition in Lysozyme

Jiayi He,

Ivan J Dmochowski

Department of Chemistry, University of Pennsylvania, Philadelphia, Pennsylvania 19104-6323, United States.

Abstract

Noble gases have well-established biological effects, yet their molecular mechanisms remain poorly understood. Here, we investigated both experimentally and computationally, the molecular modes of xenon (Xe) action in bacteriophage T4 lysozyme (T4L). By combining indirect gassing methods with a colorimetric lysozyme activity assay, a reversible, Xe-specific $(20 \pm 3)\%$ inhibition effect was observed. Accelerated molecular dynamic simulations revealed that Xe exerts allosteric inhibition on the protein by expanding a C-terminal hydrophobic cavity. Xe-induced cavity expansion results in global conformational changes, with long-range transduction distorting the active site where peptidoglycan binds. Interestingly, the peptide substrate binding site that enables lysozyme specificity does not change conformation. Two T4L mutants designed to reshape the C-terminal Xe cavity established a correlation between cavity expansion and enzyme inhibition. This work also highlights the use of Xe flooding simulations to identify new cryptic binding pockets. These results enrich our understanding of Xe-protein interactions at the molecular level and inspire further biochemical investigations with noble gases.
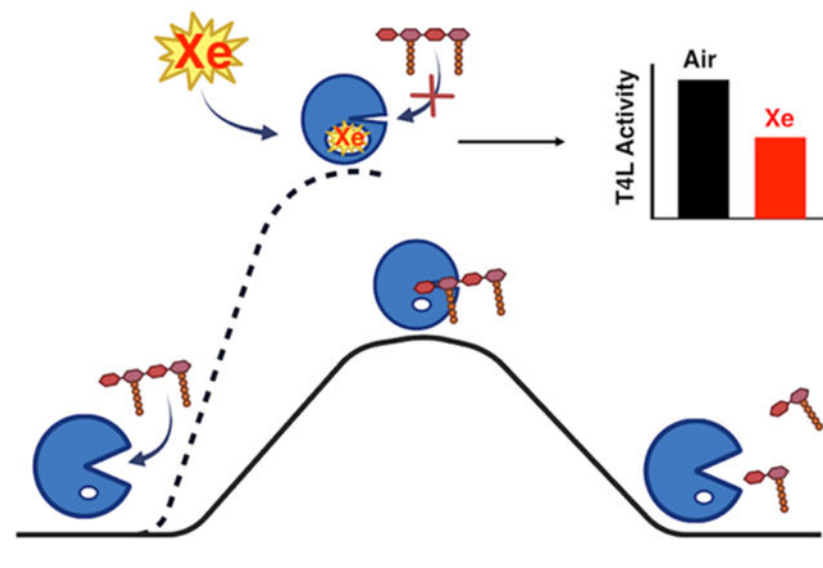
Graphical Abstract

ivandmo@sas.upenn.edu, Tel: 215.898.6459, Fax: 215.573.2112.

INTRODUCTION

Noble gases have well-documented functional activities in many biological processes, despite being chemically inert.[1] Xenon (Xe) elicits the broadest clinical interest due to its useful radiological, neuroprotective, and anesthetic properties.[2-5] The isotopes ^{129}Xe and ^{131}Xe possess $I = 1/2$ and $3/2$ nuclear spins, respectively, and are suitable for nuclear magnetic resonance (NMR) spectroscopy and imaging. The NMR chemical shift of ^{129}Xe bound to protein can vary greatly, making ^{129}Xe a promising molecular imaging probe.[6-13] Polarean's Xenoview system was recently FDA approved for generating hyperpolarized xenon and its use in human lung imaging. To date, Xe has been reported to bind to a wide range of sites in proteins, the best characterized are small hydrophobic cavities.[14] These weak but specific Xe binding interactions exert inhibitory effects on different types of proteins, e.g., xenon inhibition of membrane-bound NMDA receptors is the primary cause of Xe anesthesia.[3, 15] Other membrane proteins including GLIC[16] and MscL mechano-sensitive channel[17] also demonstrate inhibition by Xe as evidenced by 2-electrode voltage clamping[16] and patch clamping.[17] In addition, Xe inhibits various enzymes, such as CopB copper ATPase,[17] and pepsin[18] as evidenced by colorimetric activity-based assays.[17, 18] Xenon achieves many useful and interesting biological effects, and the potential for additional clinical applications motivates greater molecular-level understanding of Xe-protein interactions.

Xe can inhibit a variety of biological processes,[1] yet surprisingly little is known about how Xe exerts these effects. One of the challenges of studying Xe-protein interactions is that Xe gas is difficult to integrate with aqueous biochemical assays. Introduction of Xe into protein solutions requires careful experimental design to maintain native protein structure. A recent study emphasized the importance of indirect gassing and discovered that previously reported inhibitory effects of Xe on the enzymes tPA and UOX arose from protein damage caused by direct sparging.[19] Moreover, traditional methods for studying protein-ligand chemistry, such as isothermal titration calorimetry (ITC), surface plasmon

resonance (SPR), and fluorescence depolarization (FP), are either challenging to perform in a sealed environment (to maintain pressure of exogenous gas) or make it difficult to quantify the amount of Xe in solution. The difficulty of employing typical biophysical solution-based techniques in a gas-tight system has precluded many other studies of Xe-protein interactions at a molecular level. Static structural analysis techniques such as protein X-ray crystallography have proven insufficient as hyperbaric conditions are required to achieve useful site occupancy. In several published examples, such as porcine pancreatic elastase, T4 lysozyme (T4L), hemoglobin, albumin, and myoglobin, Xe binding minimally perturbed the crystallized protein structure.[20-26]

Herein, we used bacteriophage T4L as a model system to study the impact of Xe on protein activity, both experimentally and computationally. T4L is a well-studied enzyme[27-30] that facilitates phage infection by breaking down the bacterial cell wall and promoting the release of virus.[31] This is a concerted process where the peptide side chain is recognized by C-terminal helices, and the β-1,4 glycosidic bond–between the repeating N-acetylmuramic (NAM) and N-acetylglucosamine (NAG) units that make up the cell wall peptidoglycan–is hydrolyzed at the active site.[32, 33] In the catalytic cycle, lysozyme smoothly and continuously changes between "open" and "closed" conformations: substrate binding induces a change from open to closed conformation to initiate hydrolysis of the glycosidic bond.[33-38] Once the bond is broken, enzyme/product complex adopts a more compact conformation and then the lysozyme "open form" is regenerated upon product release.[36] Approximately 10% of lysozyme molecules are transiently paused at intermediate states between open and closed conformations when misalignment of substrate occurs.[35] T4L is a small globular protein composed of five major α-helices and three β-sheets that are connected by free loops (Figure 1). The C-terminal domain, spanning from helices D to J, is connected by 3_{10} helices and contains a unique and well-characterized internal cavity. Point mutations inside this cavity, such as L133F and A129V, were used to study the hydrophobic packing effect inside protein.[39] Other point mutations including L99A, L121A, L133A, and F153A, have been used to enlarge the cavity size, allowing T4L to serve as a paradigm for studying protein-ligand chemistry.[40-42] Xe binding to the C-terminal cavity in various mutants of T4L has been established by X-ray crystallography and NMR studies,[43, 44] but the effect of Xe binding on lysozyme activity has not been investigated previously. This study is the first to report an inhibitory effect of Xe on the T4L system, and the first to provide a molecular mechanism that can explain Xe inhibition in a small model protein. This work identifies surprising features linking Xe-protein binding to protein activity.

Materials and Methods

Plasmid Preparation.

The clone encoding pseudo-wildtype T4 lysozyme (WT*) was obtained from Addgene (plasmid #18111) developed in the laboratory of B. Matthews. T4L(WT*) is a cysteine-free lysozyme with the C54T and C97A substitutions made to the wildtype T4 lysozome (UniProt P00720). Mutations were introduced to the T4L(L99A) (also cysteine-free) gene *via* site-directed mutagenesis using the forward and reverse primers, as listed in Table S1. The mutated plasmids were amplified in NEB-5α competent *E. coli* cells and purified using

Miniprep Kit (New England Biolabs). Then the plasmids were analyzed at the University of Pennsylvania Sequencing Facility to verify mutations. The gene encoding cysteine-free T4L(A129V/L133F) mutant was synthesized and cloned into pUCIDT-Amp Goldengate Ampicillin vector followed by DNA sequencing to confirm the mutation.

Protein Expression and Purification.

Lysozymes were transformed into BL21(DE3) competent *E. coli* cells (New England Biolabs). The cells were grown in 3×1 L of LB Miller broth with 100 μg/mL ampicillin. The protein expression was induced by adding IPTG to a final concentration of 1 mM to the cell culture at an OD of 0.8-1.0. Cells were incubated and harvested within 90 min at 30 °C, pelleted by centrifugation, and stored at −80 °C. Frozen cells were resuspended in lysis buffer containing 25 mM MOPS, 25 mM Tris, 10% glycerol, 1 mM PMSF, pH 7.6. Cells were treated with benzonase nuclease (Sigma) and 1 mM $MgSO_4$ to reduce the viscosity of the lysate. After stirring the suspension on ice for 30 min, cells were sonicated on ice to disrupt the bacterial cell wall and release the protein into the buffer. The lysates were clarified by centrifugation, and supernatants were collected for further purification. Proteins were purified on CM Sepharose cation exchange resin, washed with 50 mM NaCl, and eluted with 220 mM NaCl. The eluent was concentrated and further purified by size exclusion chromatography in 30 mM sodium phosphate and 200 mM NaCl buffer using a HiLoad 16/600 Superdex column (GE Life Sciences). Fractions containing pure protein were pooled and concentrated. Protein concentration was determined from the absorbance at 280 nm (ε_{280} = 25,440 M^{-1} cm^{-1}). The same procedure was carried out for the expression and purification of all T4L variants. Protein identity and purity were confirmed by SDS-PAGE and MALDI-TOF-MS (Figures S1, S2). Protein structure was confirmed by circular dichroism (CD) spectroscopy (Figure S3).

Indirect Gassing.

An indirect gassing method was used to prepare Xe-saturated protein solution and avoid denaturation (Figure 2). The buffer solution was degassed through high vacuum line via a 16-gauge Air-Tite needle inserted through the septum into the headspace. After degassing was complete, a 22-gauge Air-Tite needle was exchanged and inserted to the bottom of the vial to allow Xe gas to be bubbled into the buffer for at least 3 min, with a 21-gauge Air-Tite needle inserted at the top to vent the excess pressure.[45] Then the protein solution (<10% in volume) was titrated into the Xe-saturated buffer through a 22-gauge Air-Tite needle with a suitable Hamilton syringe to make Xe-saturated protein sample. Estimated Xe concentration in final protein solution was roughly 90% of saturated Xe concentration of 5.05 mM, equivalent to 4.5 mM at 1 atm. The final protein solution was incubated for 30 min to allow equilibration before use. N_2-saturated protein was prepared using the same procedure.

Spontaneous Degassing.

Degassing of Xe from Xe-saturated protein solution was completed by opening the septum cap and allowing air to exchange for at least 30 min, then covering with parafilm and storing at 4 °C for at least 4 h to allow air to continue equilibrating with the solution. This spontaneous air exchange prevented protein damage caused by sparging and degassing.

Activity Assay in a Sealed Environment.

Lysozyme activity was measured as previously described[46] using lyophilized *Micrococcus lysodeikticus* (Sigma) cells resuspended at 0.15 mg/mL in 30 mM sodium phosphate buffer (pH 7.2) and monitoring the decrease of OD_{450} nm via Agilent Cary 3500 UV-Vis Multicell Peltier spectrophotometer. Xe-saturated protein was prepared as previously described using the indirect gassing approach. To ensure a Xe-saturated environment during the reaction, Xe-saturated *Micrococcus lysodeikticus* suspensions were also prepared by degassing of air followed by gassing with Xe (Figure 2). To start the activity assay, 300 μL of Xe-saturated lysozyme was delivered into a 1 cm-wide quartz cuvette with a septum cap (Sterna Cells) that contained 2.7 mL of /Xe-saturated *Micrococcus lysodeikticus* cell suspension through a 22-gauge, 4-inch Air-Tite needle with a suitable Hamilton syringe. The reaction was mixed immediately by quickly inverting the cuvette three times and the activity was measured by monitoring the continuous change in absorbance at 450 nm at 25 °C without stirring. A blank measurement by titrating buffer instead of protein was also performed as a control. Enzymatic activity was recorded as activity unit, defined by the initial rate of change (slope measured in the first minute) in OD_{450} per minute at pH 7.2 and 25 °C. This activity assay was repeated three times for each concentration of T4L in air and in Xe. N_2 was also introduced as a control gas using the same procedure described above.

Circular Dichroism (CD) Spectroscopy.

CD spectra of all three T4L variants (WT*, L99A, A129V/L133F) with and without Xe were collected on a Jasco J-1500 CD spectrometer equipped with a Peltier temperature controller. Spectra were measured from 10 μM protein in 30 mM sodium phosphate and 200 mM sodium chloride (pH = 7.2) buffer inside a quartz cuvette with a 1 mm path length. Spectra were taken at 25 °C with a wavelength step of 1 nm.

Mass Spectrometry.

MS spectra were carried out on a Bruker Microflex LRF matrix-assisted laser desorption/ionization -time of flight (MALDI-TOF) mass spectrometer (MS). The matrix used was a saturated solution of sinapinic acid in 70% acetonitrile with 0.1% trifluoroacetic acid.

Molecular Dynamics (MD).

MD simulations were performed with NAMD 2.14 software[47] using the Bridges-2 Regular Memory system at the Pittsburgh Supercomputing Center (PSC).[48, 49] Two different simulation approaches were used in this study to compare the effects of Xe on protein dynamics. The first approach, Xe-free simulations, was initiated with the protein in the absence of xenon to study free protein dynamics. Initial structures of T4L(WT)* and L99A were obtained from crystal structures (PDB codes: 1L63, 1L90). A129V/L133F was generated using PyMOL based on the L133F crystal structure (PDB code: 1P64). The second approach, Xe flooding simulations, created a highly concentrated Xe pool (146 mM) in surrounding solvent to allow Xe atoms an opportunity to diffuse into the protein and provide a detailed analysis of Xe-protein interactions. The Xe parameterization published by Verlet et al. was used.[50] In each simulation, protein was solvated in a TIP3P water box[51] and 150 mM NaCl was used to neutralize total charge. The energy of each

system was minimized with 1,000 steps, after which the system was equilibrated at a temperature of 300 K and a pressure of 1 atm using the Langevin thermostat and barostat methods. The CHARMM36 force field was used to perform all MD simulations.[52] The Xe atom was treated with only non-bonded interactions.[50] Periodic boundary conditions were employed, and the SHAKE algorithm was applied to constrain the lengths of all bonds that involve a hydrogen.[53] Both approaches used the accelerated MD (aMD) simulation method adopted from Duan et al. 2019 to overcome the computer speed limitation.[54] A robust bias potential energy was added to the actual potential energy to reduce the heights of local energy barriers, allowing a more efficient simulation using limited computing power. A 0.6 ns simulation was used to generate aMD parameters for boost potentials as previously described.[54] All aMD parameters are shown in Table S2. MD trajectories of at least 130 ns were obtained from each simulation with 0.2 ns step size. Xe occupancy, internal cavity analyses, conformational changes, and Cα torsion angle analysis, were performed using VMD 1.9.3.[53]

Xe Occupancy Analysis.

Xe occupancy map was generated by calculating the average number of Xe atoms bound within 4 Å to any atom of the protein. The number of bound Xe atoms at 1) the N-terminal T4L active site, 2) the C-terminal T4L primary Xe binding site, and 3) a newly discovered cryptic site was plotted against simulation time for each T4L mutant (Figure S5, Table S3).

Internal Cavities Analysis.

Internal hydrophobic cavities were detected and analyzed by MDpocket algorithm,[55] which traces cavities of interest over MD trajectories based on Voronoi tessellation. Solvent molecules and Xe atoms were stripped away from the MD simulations, and protein backbone structural alignment was carried out using VMD 1.9.3. MDpocket-defined cavity analysis relies on the concept of α-spheres – a sphere that contacts four atoms on its boundary and contains no internal atom.[56] High hydrophobicity (-p 0.99) and small probe size (-i 5) were used to define internal hydrophobic cavities in T4L variants. The percentage of detectable cavities (number of frames that have detectable cavities/total frames) in the simulation time and the average cavity volume are summarized in Table 1.

Conformational Change Analysis.

The percentage of each T4L variant in the closed conformation in the simulation time was analyzed. The closed conformation was defined by the formation of the inter-domain salt bridge (E22-R137) at a cut-off donor-to-acceptor distance of 3.6 Å (Figure 3). The distribution of salt-bridge distances was included in Figure S6.

Cα Torsion Angle Analysis.

Cα torsion angles were calculated to identify dynamic protein backbone changes upon Xe binding. Cα torsion angles were defined by two values: φ and ψ. For each residue i, φ is the rotation angle between the Cα(i) and N(i) bond in the Cβ(i-1)-N(i)-Cα(i)-Cβ(i) plane, and ψ is the rotation angle around the Cα(i) and Cβ(i) bond in the N(i)-Cα(i)-Cβ(i)-N(i+1) plane. The Cα torsion angle differences for each residue were calculated over MD

trajectories and plotted by subtracting the torsion angles for the Xe flooding simulation from those in the Xe-free simulation. The Cα torsion angles for open and closed conformations of T4L were calculated based on the crystal structures (PDB for open conformation: 172L, PBD for closed conformation: 3LZM). The difference map was plotted by subtracting the torsion angles for the closed conformation from those in the open conformation for each residue.

RESULTS

Xe Inhibition on T4L Variants.

The catalytic activity of different T4L mutants was investigated under gassing (air, N_2, and Xe) and degassing conditions to examine the effect of Xe on enzyme activity and the potential for enzyme recovery after Xe removal. For T4L(WT*), no significant changes in activity were observed when N_2 was introduced compared to the activity measured in air, $(101 \pm 5)\%$. In contrast, a $(20 \pm 3)\%$ inhibitory effect was observed in the presence of Xe and this activity was recovered after degassing to achieve $(103 \pm 2)\%$ of the original value (Figure 4).

Based on the results of the simulation analysis that Xe inhibition is associated with cavity size, two T4L mutants that were previously characterized with different cavity size were expressed, purified, and tested: A129V/L133F, which has a side-chain-occupied cavity,[39] and L99A, which possesses an enlarged cavity capable of accommodating three Xe atoms.[43] In A129V/L133F, similar inhibition and recovery effects were detected with a $(19 \pm 2)\%$ decrease in activity in the Xe-saturated system, and $(95 \pm 4)\%$ recovery after Xe degassing, and no significant changes in N_2-saturated enzyme solution $(104 \pm 3)\%$ (Figure 4). Interestingly, neither N_2, $(104 \pm 6)\%$, nor Xe, $(103 \pm 6)\%$, had observable effects on L99A activity when compared to the activity measured in air (Figure 4). To confirm this Xe-specific inhibition effect was a general feature of T4L, the activity at various enzyme concentrations (1 to 9 μg/mL) in air and Xe-saturated buffer solution was investigated for each mutant. The same inhibition trend was consistently observed in WT* and A129V/L133F in the presence of Xe, but no changes were observed in L99A (Figure 5).

CD Analysis.

CD spectra for all mutants were collected before and after gassing (Figure S3). All spectra before and after degassing share a similar CD trace and similar molar ellipticity at 222 nm (α-helix) and 218 nm (β-sheet) compared to WT*, suggesting a preserved secondary structure regardless of the presence of mutations or xenon. The thermal stability of L99A and A129V/L133F decreased by 12.0 °C and 5.3 °C respectively, compared to the WT* melting temperature, $T_m = 53.8 \pm 0.3$ °C (Figure S4). These melting temperatures agreed with the previously reported T_m values for WT* (51.8 °C) and L99A (36.1 °C),[57] providing evidence that all variants maintain stable structures when performing activity assays in solution at 25 °C. Changes in protein thermal stability were insignificant in the presence of xenon (data not shown).

Molecular Dynamics.

An aMD simulation of at least 130 ns was obtained for each T4L variant (WT*, L99A, and A129V/L133F) using both Xe-free and Xe-flooding approaches. Xe was observed to exchange between aqueous solvent and the internal hydrophobic cavities in all three variants during the Xe flooding simulations.

Xe Occupancy Map.

The interaction between Xe and T4L was previously identified using structural methods, including X-ray crystallography and proton NMR, which showed evidence of direct binding inside C-terminal internal cavity and strong interactions at helix C (Figure 1).[43, 44] In order to verify these interactions in simulation results, Xe occupancy maps were generated from Xe flooding simulations for each T4L variant. The maps showed that Xe has highest affinity at the C-terminal helices, and low affinity at the active site protein (residues E11, D20, and T26) (n < 0.05) (Figure 6a, b). In WT*, high-affinity residues with n > 1.0 (residues M102, V111, F114, L118, and L133) (Figure 6a) coincide with residues in Xe binding sites identified in X-ray crystal structure (PDB: 1C6T) and proton NMR analysis.[43, 44] A129V/L133F also has similar high-affinity sites with n > 1.0, except that V111 has a slightly lower affinity of n = 0.8 (Figure 6a, b). The Xe binding site in L99A shifted towards residues L118, V87, and L99 with Xe affinity n > 0.7 (Figure 6a, b). Interestingly, the simulation results revealed that more Xe atoms were bound to the primary Xe binding cavity in WT* and A129V/L133F, compared to the L99A variant (Figure S5, Table S3). This contradicts the prediction from crystallography, which suggested that L99A would bind more Xe atoms and either A129V or L133F would be too occupied to bind with ligands.[39, 43] However, it is important to note that X-ray crystallography applied 8 atm pressure to force Xe to bind with L99A, and no Xe binding experiments were tested for A129V/L133F. Our simulation results highlighted the dynamic interactions between T4L variants and Xe atoms, providing a new perspective on possible binding behaviors between Xe and T4L. Moreover, an additional cryptic site with high Xe occupancy located at helices C, D, and E (residues V75, I78, L84, I100, V104, and E108) was observed in all three variants, with highest Xe occupancy in WT* (4.29 bound Xe atoms, Figure 6a, S5, Table S3), and fewer bound Xe atoms in L99A and A129V/L133F, 1.50 and 0.88, respectively (Table S3). Among these residues, residues V78, I78, and E108 located at helix C were identified to have strong Xe interactions in NMR experiments, [43] but no binding site in this region was identified.

Internal Cavity Analysis.

The percentage of detectable cavities and their volumes increased in all three T4L proteins in Xe flooding simulations compared to Xe-free simulations. Among the three variants, WT* had the largest increase with 81.6% more detectable cavities and a 121 Å³ increase in total average cavity volume (Table 1). A129V/L133F showed a similar increase (65.0%) in detectable cavities with a 22.5 Å³ increase in volume (Table 1). L99A was least perturbed by xenon flooding, with only a 33% increase in detectable cavities, and 11.2 Å³ increase in cavity volume (Table 1).

Conformational Change Analysis.

In WT*, 24.5% more of the simulated protein structures were in a closed conformation in the presence of Xe, and 12.3% more of the A129V/L133F simulated structures were in a closed state in the presence of xenon. In contrast, 34.9% more of the L99A simulated structures were in the open conformation in the presence of xenon. The corresponding data are summarized in Table 2.

Cα Torsion Angle Analysis.

To locate significant changes of the main-chain structure of T4L variants in the presence of Xe, the Cα torsion angle difference of each residue was plotted for each variant (Figure 7).[58] The largest Cα torsion angle differences were observed for three different types of main-chain structures: active site, free loops, and 3_{10} helices near Xe binding site (Figure 7a, b). Changes in active-site conformation revealed a large contribution from E11 and D20 in both WT* and A129V/L133F, but only D20 in L99A (Figure 7c). In WT*, torsion angles from ψ (11, 20), and φ (12, 20, 21) were largely responsible. In A129V/L133F, alterations in ψ (12, 20), and φ (20, 21) were the most important. However, in L99A, only ψ (20) made a significant contribution. Changes in free loops were found at G30, T34, and T157 (Figure 7c). G30 is located at the free loop inside the active-site pocket in T4L, whereas T34 and T157 are located at free loops that were solvent exposed (Figure 7c). In WT*, the torsion angles arising from φ (30) and ψ (157) represent the largest changes; in A129V/L133F, φ (34) changed the most; and in L99A, φ (34, 157) and ψ (157) showed the largest alterations (Figure 7c). Changes in 3_{10} helices near a Xe binding site were mainly found at residues L84, S90, L91, M106, G107, and V111 to F114. The 3_{10} helix is a variation where three amino acids are found in one turn compared to four in a standard α-helix. It occurs at the turning point of α-helices in T4L (Figure 7c). In WT*, ψ (90, 106, 112, 114), and φ (84, 91, 106, 107, 111, 113, 114) contributed the most to the changes in torsion angles; in A129V/L133F, φ (106) and ψ (107) demonstrated the largest changes. In L99A, ψ (107) remained as the largest difference, however, the value was half of that in A129V/L133F (Figure 7c).

DISCUSSION

Previous studies of Xe-enzyme interactions provided few mechanistic hypotheses to explain the biological effects that Xe can exert on protein function. Here we reported Xe-specific inhibition of 20% on the activity of T4L(WT*). Experiments employed an indirect gassing method to avoid protein denaturation (Figure 4) and were interpreted using aMD simulations to reveal global protein dynamic changes induced by the binding of a few Xe atoms at the C-terminal hydrophobic cavity (Figure 6). Experiments and simulations were conducted with three T4L variants, which provided additional hypothesis testing and cross-validation.

Xe-specific Allosteric Inhibition.

CD structural analysis confirmed a similar secondary structure after gassing (Figure S3). Control studies with N_2 (a smaller, less polarizable gas molecule) revealed no activity changes, which confirmed that the observed inhibition is a Xe-specific effect and not a consequence of the gassing procedure (Figure 4). Xe inhibitory effect on T4L(WT*) is

also a reversible process as enzyme activity can be fully recovered after removal of Xe (Figure 4). These observations raise the question of how Xe exerts an inhibitory effect on T4L(WT*) without inducing experimentally observable structural changes. To understand the mechanism of this inhibitory effect, we first need to clarify how Xe binds to the protein. As the nature of the noble gas is to occupy small hydrophobic cavities, a high Xe occupancy (n > 1.0) was detected in Xe flooding simulations at residues that coincide with a hydrophobic cavity (M102, V111, F114, L118, and L133) previously determined by X-ray crystallography (Figure 6a).[43] Interestingly, an extremely low Xe occupancy (n < 0.05) was observed at the T4L active site (E11, D20, and T26) (Figure 6a), probably due to the high solvent accessibility of these active-site residues (Figure S7). Because the C-terminal Xe binding site is far from the N-terminal active site (>17 Å) (Figure 6c), competitive inhibition of Xe at the active site seems impossible. Such high occupancy at the Xe binding site and low occupancy at the active site suggest an allosteric inhibition mechanism.

Xe Binding Promotes an Inactive Closed Conformation.

To explore how a small cavity with high Xe occupancy affects the overall protein dynamics, MDpocket analysis[55] was carried out to calculate dynamic changes of cavity volumes. The increase in the percentage of structures with detectable cavities and the increase in their volumes (Table 1) both suggest that Xe occupancy of the hydrophobic site, as indicated in the Xe occupancy map (Figure 6a), expanded the cavity volume. This expansion is in agreement with observations in protein crystal structures where cavity volume progressively increases from unliganded cavity (PDB: 1L63) to the Xe complexes (PDB: 1C6T) with minimal changes to the backbone structure (RMSD = 0.161 Å).[43] A similar phenomenon was observed for a series of small-molecule host-guest complexes, where Xe binding measurably expanded the cavity volume in the solid-state.[59]

Hinge-bending motion and substrate-induced conformational transition of T4L in solution is a key element in lysozyme catalysis.[33-38] To investigate how Xe-binding-induced cavity expansion is associated with enzymatic activity changes, we first examined overall conformational changes of T4L upon Xe binding. The domain closure of T4L was evaluated by the formation of an inter-domain salt bridge (E22-R137) and compared in the absence and presence of Xe (Figure 3). We observe that protein preferentially remains in the open state in the absence of Xe and substrate (Table 2), as previously indicated by electron paramagnetic resonance (EPR) spectroscopy,[34] single-molecule nanocircuit,[35] fluorescence spectroscopy,[36] and paramagnetic NMR spectroscopy.[38] These techniques indicated that the structure of T4L is on average more open in solution than suggested by the closed conformation of the crystal structure. More importantly, high Xe occupancy in the C-terminal site is found to promote the cleft closure of T4L(WT*) (Table 2). Because Xe mainly interacts with the hydrophobic residues in the C-terminal cavity (Figure 6), we hypothesize that the protein adopts this relatively high-energy (closed) state as a result of the large internal cavity expansion as Xe "squeezes" into the binding cavity. The increased population of closed conformations can impede lysozyme from accessing substrate and thereby affect the series of "open"- "closed"-"fully closed"-"open" conformational changes induced by substrate binding in the lysozyme catalytic cycle.[36] As prior studies also revealed ligand-induced allostery intrinsic to all proteins and a conformation-dependent mechanism

for Xe inhibition of the NMDA-receptor,[15, 60] our findings on the conformational changes induced by Xe binding provide a compelling Xe inhibition mechanism at the molecular level.

Active Site Distortion Through Long-range Transduction.

To localize residues that change upon Xe-induced conformational changes of T4L(WT*), a torsion angle difference map, inspired by Björkman and Mowbray's analysis of the conformational changes of ribose binding protein (RBP),[58] was generated. Interestingly, the active-site residue E11 demonstrates the largest distortion, with a ψ of 83.6° and φ of −14.7° (Figure 7), whereas residues involved in the recognition of the short peptide that contributes to enzyme specificity, N116, S117 (helix G), N132, K135 (helix H), and R137 (helix I) via hydrogen bonding,[61] show minimal changes (Figure 7). As T4L catalysis depends on both peptidoglycan binding at the active site for catalysis to occur and peptide binding at the C-terminal helices for enzyme specificity, [35, 37] our data further suggest that substrate accessibility can be lowered by the presence of Xe, and this decreased affinity likely comes from the distortion of the peptidoglycan binding site at the active site rather than the short peptide binding site, as a result of the Xe-induced global conformational changes. Other significant changes are located at either free loops of the protein (G30, T157) that connect helix-helix or helix-sheet structure, or at the 3_{10} helix turning points (L84, S90, L91, M106, G107, V111 to F114) between helices E and F that comprise part of the Xe binding site (Figure 7). These relatively less stable 3_{10} helices undergo backbone distortions in response to Xe-binding cavity expansion, and the dynamic change is then transduced from the Xe-binding site through 3_{10} helices to the active site through the connection of free-loops, causing a distortion at the active site towards the peptidoglycan. Imperfect alignment of substrate at the active site reduces its binding and therefore leads to a decrease in lysozyme activity.

Xe Inhibition Correlates with Cavity Expansion.

To test our hypothesis that the global conformational changes and active-site distortion arise from Xe-induced pocket expansion, two variants that have been shown by X-ray crystallography to have either an enlarged binding pocket (L99A)[43, 62, 63] or a side-chain-occupied pocket (A129V/L133F)[39] were investigated. MDpocket analysis confirmed that L99A possesses an enlarged cavity with higher detectable frequency, and A129V/L133F possesses a smaller cavity with lower detectable frequency compared to WT* (Table 1). As predicted, L99A with large binding cavity experiences less cavity expansion upon Xe binding (Table 1). However, A129V/L133F that was designed to not bind with Xe because of the small cavity, still experiences a large cavity expansion when Xe "squeezes" in (Table 1). Protein flexibility in solution enables the hydrophobic cavities to expand and allow Xe binding. Remarkably, L99A with a smaller cavity volume increase in the presence of Xe demonstrates no statistically significant changes in enzyme activity (Figure 4, 5), whereas A129V/L133F with a larger pocket expansion upon Xe binding experiences a 19% inhibitory effect from Xe (Figure 4), analogous to WT*.

To explore further the Xe inhibitory effect on L99A and A129V/L133F at the molecular level, Xe occupancy at the surface of the protein, conformational changes of lysozyme, and

Cα torsion angle for each residue were analyzed for the two mutants. The Xe occupancy map suggests a stronger binding at C-terminal helices in A129V/L133F than in L99A (Figure 6). The conformational analysis reveals that Xe enhances cleft closure in A129V/L133F in a similar manner as that in WT* but promotes cleft opening in the L99A variant (Table 2). This discrepancy in different variants can be explained by the different degrees of cavity expansion upon Xe binding. As Xe occupancy tends to expand the binding cavity in WT* and A129V/L133F, these proteins adopt a relatively high-energy (closed) state as a result of the large internal cavity expansion. Whereas in L99A, Xe is well accommodated by the existing cavity, and expands the cavity to a lesser degree. Therefore, the L99A protein preferentially remains at a relatively low energy (open) state in the presence of Xe. When more enzyme is in the open state in the presence of Xe, as in L99A, accessibility to the substrate is not rate-limiting, and hence no obvious changes in enzymatic activity were observed. The torsion angle difference map shows a larger distortion near active-site residue E11 in A129V/L133F than in L99A (Figure 7), which suggests a larger transduced effect in A129V/L133F and explains the higher degree of inhibition. Notably, the torsion angle of D20, another important residue in the active site, changes in both mutants and in WT*, but does not have a significant impact on the activity of L99A. This is possibly because E11 plays a more crucial role than D20 in the catalytic mechanism. In the catalysis reaction, E11 acts as an acid to donate a proton to the glycosidic bond, and D20 acts as a base to remove a proton from water and makes water a better nucleophile to attack the glycosidic bond (Figure S8). Although this was shown previously to be a one-step mechanism where E11 and D20 act simultaneously to form the intermediate,[33] E11 is deprotonated at neutral pH in our activity assay, thereby making proton donation a rate-determining step. Moreover, D20 has been shown to be more tolerant of mutations, e.g., D20C has nearly identical activity as WT*, but mutations at E11 completely abrogated activity.[64-67] In addition, T26, a third residue at the catalytic site, exhibits minimal torsion angle changes ($Cα < 3°$) in all T4L variants, indicating the minimal effect at this site upon Xe binding. In the catalytic reaction, T26 does not participate in the chemistry of cleaving glycosidic bonds but acts to stabilize the deprotonated water,[33, 67] suggesting a relatively minor role compared to E11. Thus, regardless of any distortions at D20 and T26, only changes near E11 contribute to the activity of T4L towards *M. lysodeikticus.* Meanwhile, the torsion angle difference map of A129V/L133F demonstrates smaller but similar deformation at 3_{10} helices in the C-terminal domain compared to that of WT*, mainly at M106 and G107, implying a similar transducing effect of Xe binding through these 3_{10} helices to the active site. L99A demonstrated the smallest 3_{10} helix distortions, consistent with the smallest cavity volume expansion upon Xe binding, and minimal impact on activity in the Xe-saturated system. Our results provide an explanation for how Xe exerts long-range inhibitory effects on T4L, improving our understanding of general Xe-protein interactions, and suggesting further avenues for investigating the complicated biological roles of Xe.

Cryptic Site Buried in T4 Lysozyme.

Interestingly, Xe flooding experiments reveal a new cryptic site in T4L(WT*) located between helices E and C, surrounded by residues V75, I78, L84, I100, V103, and E108 (Figure 6). This cryptic site is also observed in the L99A and A129V/L133F mutants, but with fewer average bound Xe atoms per residue compared to WT* (Figure S5, Table S3).

This cryptic site is thought to be innocent in lysozyme activity because it does not possess dihedral angle changes upon Xe binding (Figure 7). Static structural tools have demonstrated a strong interaction between this site and Xe but have not reported it as a binding site. Previous ^{1}H NMR studies on T4L(WT*) revealed similar chemical shifts under Xe pressure at residues V75 and I78 to that of residues within the Xe binding site, and spin polarization induced Nuclear Overhauser Effect (SPINOE) studies detected not only enhanced proton signals at the primary Xe binding site but also at I78 and E108.[44] Our simulation results and the prior NMR experiments indicate high-occupancy Xe binding at this cryptic site that was previously underappreciated. Identifying cryptic sites in proteins has long been a challenge because of their invisibility in the absence of ligands.[68-71] Although the biological function of this cryptic site remains unknown and requires further investigation, this finding supports the possibility of employing Xe flooding simulations in search of not only internal cavities[72] in proteins but also new cryptic sites that could potentially be targeted with higher-affinity ligands.

CONCLUSION

In summary, we have demonstrated that Xe has a reversible inhibitory effect in the T4L system and revealed the relationship between the C-terminal hydrophobic cavity size of T4L and the effect of Xe on its activity. Our results strongly suggest that Xe can not only "squeeze into" and expand pre-existing small protein cavities but also dynamically promote the formation of new cavities, which differs from the picture that has often emerged from X-ray crystallography, showing xenon binding to a small number of static hydrophobic sites.[6, 43, 44] Remarkably, the cavity expansion induced by the binding of a small cluster of Xe atoms near the C terminus promotes an overall, global closed conformation and induces dynamic changes in the protein, which are then transduced through a series of 3_{10} helices to the active site, leading to a large distortion at the active site that affects substrate accessibility and alignment. This work also highlights strong potential for using Xe flooding simulations to probe new cryptic binding sites in small proteins. These findings enrich our understanding of Xe-protein interactions at the molecular level and motivate further investigation of the effects of noble gases in Biochemistry and Medicine.

Supplementary Material

Refer to Web version on PubMed Central for supplementary material.

ACKNOWLEDGMENTS

REFERENCES

(1). Winkler DA; Thornton A; Farjot G; Katz I The Diverse Biological Properties of the Chemically Inert Noble Gases. Pharmacol. Ther 2016, 160, 44–64. [PubMed: 26896563]

(2). Cullen SC; Gross EG The Anesthetic Properties of Xenon in Animals and Human Beings, with Additional Observations on Krypton. Science 1951, 113 (2942), 580–582. [PubMed: 14834873]

(3). Franks NP; Dickinson R; de Sousa SLM; Hall AC; Lieb WR How Does Xenon Produce Anaesthesia? Nature (London) 1998, 396 (6709), 324. [PubMed: 9845069]

(4). Mugler JP; Altes TA Hyperpolarized 129Xe MRI of the Human Lung. J. Magn. Reson 2013, 37 (2), 313–331.

(5). Liu W; Liu Y; Chen H; Liu K; Tao H; Sun X Xenon Preconditioning: Molecular Mechanisms and Biological Effects. Med. Gas Res 2013, 3 (1), 3. [PubMed: 23305274]

(6). Rubin SM; Lee S-Y; Ruiz EJ; Pines A; Wemmer DE Detection and Characterization of Xenon-Binding Sites in Proteins by 129Xe NMR Spectroscopy. J. Mol. Biol 2002, 322 (2), 425–440. [PubMed: 12217701]

(7). Wang Y; Roose BW; Palovcak EJ; Carnevale V; Dmochowski IJ A Genetically Encoded β-Lactamase Reporter for Ultrasensitive 129Xe NMR in Mammalian Cells. Angew. Chem., Int. Ed 2016, 55 (31), 8984–8987.

(8). Mari E; Berthault P 129Xe NMR-based Sensors: Biological Applications and Recent Methods. Analyst (London) 2017, 142 (18), 3298–3308. [PubMed: 28831479]

(9). Roose BW; Zemerov SD; Dmochowski IJ Nanomolar Small-Molecule Detection using a Genetically Encoded 129Xe NMR contrast agent. Chem. Sci 2017, 8 (11), 7631–7636. [PubMed: 29568427]

(10). Roose BW; Zemerov SD; Wang Y; Kasimova MA; Carnevale V; Dmochowski IJ A Structural Basis for 129 Xe Hyper-CEST Signal in TEM-1 β-Lactamase. ChemPhysChem 2019, 20 (2), 260–267. [PubMed: 30151973]

(11). Zemerov SD; Roose BW; Farenhem KL; Zhao Z; Stringer MA; Goldman AR; Speicher DW; Dmochowski IJ 129Xe NMR-Protein Sensor Reveals Cellular Ribose Concentration. Anal. Chem 2020, 92 (19), 12817–12824. [PubMed: 32897053]

(12). Zhao Z; Roose BW; Zemerov SD; Stringer MA; Dmochowski IJ Detecting Protein–Protein Interactions by Xe-129 NMR. Chem. Commun 2020, 56 (75), 11122–11125.

(13). Zhao Z; Rudman NA; He J; Dmochowski IJ Programming Xenon Diffusion in Maltose-Binding Protein. Biophys J 2022. From NLM.

(14). Prangé T; Schiltz M; Pernot L; Colloc'h N; Longhi S; Bourguet W; Fourme R Exploring Hydrophobic Sites in Proteins with Xenon or Krypton. Proteins: Struct. Funct. Genet 1998, 30 (1), 61–73. [PubMed: 9443341]

(15). Liu LT; Xu Y; Tang P Mechanistic Insights into Xenon Inhibition of NMDA Receptors from MD Simulations. J. Phys. Chem. B 2010, 114 (27), 9010–9016. [PubMed: 20560662]

(16). Weng Y; Yang L; Corringer P-J; Sonner JM Anesthetic Sensitivity of the Gloeobacter violaceus Proton-Gated Ion Channel. Anesth. Analg 2010, 110 (1), 59–63. [PubMed: 19933531]

(17). Petrov E; Menon G; Rohde PR; Battle AR; Martinac B; Solioz M Xenon-Inhibition of the MscL Mechano-Sensitive Channel and the CopB Copper ATPase under Different Conditions Suggests Direct Effects on these Proteins. PloS one 2018, 13 (6), e0198110–e0198110. [PubMed: 29864148]

(18). Zhang L; Zhang Y; Cheng J; Wang L; Wang X; Zhang M; Gao Y; Hu J; Zhang X; Lü J; et al. Inert Gas Deactivates Protein Activity by Aggregation. Sci Rep 2017, 7 (1), 10176–10176. PubMed. [PubMed: 28860621]

(19). Cahill J; Ruffing AM Revisiting the Effects of Xenon on Urate Oxidase and Tissue Plasminogen Activator: No Evidence for Inhibition by Noble Gases. Front. Mol. Biosci 2020, 7, 574477. [PubMed: 33024747]

(20). Roose BW; Zemerov SD; Dmochowski IJ Xenon–Protein Interactions: Characterization by X-Ray Crystallography and Hyper-CEST NMR. Elsevier, 2018; pp 249–272.

(21). Mueller-Dieckmann C; Polentarutti M; Djinovic Carugo K; Panjikar S; Tucker PA; Weiss MS On the Routine Use of Soft X-rays in Macromolecular Crystallography. Part II. Data-Collection Wavelength and Scaling Models. Acta Crystallogr. D Biol. Crystallogr 2004, 60 (1), 28–38. [PubMed: 14684889]

(22). Schiltz M; Fourme R; Prangé T Use of Noble Gases Xenon and Krypton as Heavy Atoms in Protein Structure Determination. In Meth. Enzymol, Vol. 374; Elsevier Science & Technology, 2003; pp 83–119.

(23). Schiltz M; Kvick Å; Svensson OS; Shepard W; De La Fortelle E; Prangé T; Kahn R; Bricogne G; Fourme R Protein Crystallography at Ultra-Short Wavelengths: Feasibility Study of Anomalous-Dispersion Experiments at the Xenon K-edge. J. Synchrotron Rad 1997, 4 (5), 287–297.

(24). Vitali J; Robbins AH; Almo SC; Tilton RF Using Xenon as a Heavy Atom for Determining Phases in Sperm Whale Metmyoglobin. J. Appl. Crystallogr 1991, 24 (5), 931–935.

(25). Quillin ML; Matthews BW Generation of Noble-gas Binding Sites for Crystallographic Phasing using Site-directed Mutagenesis. Acta Crystallogr. D Biol. Crystallogr 2002, 58 (1), 97–103. [PubMed: 11752783]

(26). Quillin ML; Matthews BW Selling Candles in a Post-Edison World: Phasing with Noble Gases Bound within Engineered Sites. Acta Crystallogr. D Biol. Crystallogr 2003, 59 (11), 1930–1934. [PubMed: 14573947]

(27). Rosemond SN; Hamadani KM; Cate JHD; Marqusee S Modulating Long-Range Energetics via Helix Stabilization: A Case Study using T4 Lysozyme. Protein Sci. 2018, 27 (12), 2084–2093. [PubMed: 30284332]

(28). Cellitti J; Bernstein R; Marqusee S Exploring Subdomain Cooperativity in T4 Lysozyme II: Uncovering the C-terminal Subdomain as a Hidden Intermediate in the Kinetic Folding Pathway. Protein Sci. 2007, 16 (5), 852–862. [PubMed: 17400925]

(29). Cellitti J; Llinas M; Echols N; Shank EA; Gillespie B; Kwon E; Crowder SM; Dahlquist FW; Alber T; Marqusee S Exploring Subdomain Cooperativity in T4 lysozyme I: Structural and Energetic Studies of a Circular Permutant and Protein Fragment. Protein Sci. 2007, 16 (5), 842–851. [PubMed: 17400926]

(30). Llinás M; Marqusee S Subdomain Interactions as a Determinant in the Folding and Stability of T4 Lysozyme. Protein Sci. 1998, 7 (1), 96–104. [PubMed: 9514264]

(31). Nakimbugwe D; Masschalck B; Deckers D; Callewaert L; Aertsen A; Michiels CW Cell Wall Substrate Specificity of Six Different Lysozymes and Lysozyme Inhibitory Activity of Bacterial Extracts. FEMS Microbiol. Lett 2006, 259 (1), 41–46. [PubMed: 16684100]

(32). Jensen HB; Kleppe G; Schindler M; Mirelman D The Specificity Requirements of Bacteriophage T4 Lysozyme. Eur. J. Biochem 1976, 66 (2), 319–325. [PubMed: 947753]

(33). Akhterov MV; Choi Y; Olsen TJ; Sims PC; Iftikhar M; Gul OT; Corso BL; Weiss GA; Collins PG Observing Lysozyme's Closing and Opening Motions by High-Resolution Single-Molecule Enzymology. ACS Chem. Biol 2015, 10 (6), 1495–1501. [PubMed: 25763461]

(34). McHaourab HS; Oh KJ; Fang CJ; Hubbell WL Conformation of T4 Lysozyme in Solution. Hinge-Bending Motion and the Substrate-Induced Conformational Transition Studied by Site-Directed Spin Labeling. Biochemistry 1997, 36 (2), 307–316. [PubMed: 9003182]

(35). Woo SO; Oh M; Alhalhooly L; Farmakes J; Rajapakse AJ; Yang Z; Collins PG; Choi Y Different Single-Enzyme Conformational Dynamics upon Binding Hydrolyzable or Nonhydrolyzable Ligands. J. Phys. Chem. B 2021, 125 (22), 5750–5756. [PubMed: 34038124]

(36). Sanabria H; Rodnin D; Hemmen K; Peulen T-O; Felekyan S; Fleissner MR; Dimura M; Koberling F; Kühnemuth R; Hubbell W; et al. Resolving Dynamics and Function of Transient States in Single Enzyme Molecules. Nat. Commun 2020, 11 (1), 1231. [PubMed: 32144241]

(37). Choi Y; Weiss GA; Collins PG Single Molecule Recordings of Lysozyme Activity. Phys. Chem. Chem. Phys 2013, 15 (36), 14879. [PubMed: 23752924]

(38). Chen J-L; Yang Y; Zhang L-L; Liang H; Huber T; Su X-C; Otting G Analysis of the Solution Conformations of T4 Lysozyme by Paramagnetic NMR Spectroscopy. Phys. Chem. Chem. Phys 2016, 18 (8), 5850–5859. [PubMed: 26680012]

(39). Karpusas M; Baase WA; Matsumura M; Matthews BW Hydrophobic Packing in T4 Lysozyme Probed by Cavity-Filling Mutants. PNAS 1989, 86 (21), 8237–8241. [PubMed: 2682639]

(40). Feher VA; Schiffer JM; Mermelstein DJ; Mih N; Pierce LCT; McCammon JA; Amaro RE Mechanisms for Benzene Dissociation through the Excited State of T4 Lysozyme L99A Mutant. Biophys. J 2019, 116 (2), 205–214. [PubMed: 30606449]

(41). López CJ; Yang Z; Altenbach C; Hubbell WL Conformational Selection and Adaptation to Ligand Binding in T4 Lysozyme Cavity Mutants. PNAS 2013, 110 (46), E4306–E4315. [PubMed: 24167295]

(42). Baldwin E; Baase WA; Zhang X-J; Feher V; Matthews BW Generation of Ligand Binding Sites in T4 Lysozyme by Deficiency-Creating Substitutions. J. Mol. Biol 1998, 277 (2), 467–485. [PubMed: 9514755]

(43). Quillin ML; Breyer WA; Griswold IJ; Matthews BW Size versus Polarizability in Protein-Ligand Interactions: Binding of Noble Gases within Engineered Cavities in Phage T4 Lysozyme. J. Mol. Biol 2000, 302 (4), 955–977. [PubMed: 10993735]

(44). Desvaux H; Dubois L; Huber G; Quillin ML; Berthault P; Matthews BW Dynamics of Xenon Binding Inside the Hydrophobic Cavity of Pseudo-Wild-type Bacteriophage T4 Lysozyme Explored through Xenon-Based NMR Spectroscopy. J. Am. Chem. Soc 2005, 127 (33), 11676–11683. [PubMed: 16104744]

(45). Zemerov SD; Lin Y; Dmochowski IJ Monomeric Cryptophane with Record-High Xe Affinity Gives Insights into Aggregation-Dependent Sensing. Anal. Chem 2021, 93 (3), 1507–1514. [PubMed: 33356164]

(46). Shugar D. The Measurement of Lysozyme Activity and the Ultra-Violet Inactivation of Lysozyme. Biochim. Biophys. Acta 1952, 8 (3), 302–309. [PubMed: 14934741]

(47). Phillips JC; Braun R; Wang W; Gumbart J; Tajkhorshid E; Villa E; Chipot C; Skeel RD; Kalé L; Schulten K Scalable Molecular Dynamics with NAMD. J. Comput. Chem 2005, 26 (16), 1781–1802. [PubMed: 16222654]

(48). Nystrom NA; Levine MJ; Roskies RZ; Scott JR Bridges. 2015, 2015; ACM Press. DOI: 10.1145/2792745.2792775.

(49). Towns J; Cockerill T; Dahan M; Foster I; Gaither K; Grimshaw A; Hazlewood V; Lathrop S; Lifka D; Peterson GD; et al. XSEDE: Accelerating Scientific Discovery. Comput. Sci. Eng 2014, 16 (5), 62–74.

(50). Verlet L; Weis J-J Perturbation Theory for the Thermodynamic Properties of Simple Liquids. Mol. Phys 1972, 24 (5), 1013–1024.

(51). Jorgensen WL; Chandrasekhar J; Madura JD; Impey RW; Klein ML Comparison of Simple Potential Functions for Simulating Liquid Water. J. Chem. Phys 1983, 79 (2), 926–935.

(52). Best RB; Zhu X; Shim J; Lopes PEM; Mittal J; Feig M; Mackerell AD Optimization of the Additive CHARMM All-Atom Protein Force Field Targeting Improved Sampling of the Backbone ϕ, ψ and Side-Chain $\chi 1$ and $\chi 2$ Dihedral Angles. J. Chem. Theory Comput 2012, 8 (9), 3257–3273. [PubMed: 23341755]

(53). Ryckaert J-P; Ciccotti G; Berendsen HJC Numerical Integration of the Cartesian Equations of Motion of a System with Constraints: Molecular Dynamics of n-Alkanes. J. Comput. Phys 1977, 23 (3), 327–341.

(54). Duan L; Guo X; Cong Y; Feng G; Li Y; Zhang JZH Accelerated Molecular Dynamics Simulation for Helical Proteins Folding in Explicit Water. Front. Chem 2019, 7, 540–540. [PubMed: 31448259]

(55). Schmidtke P; Bidon-Chanal A; Luque FJ; Barril X MDpocket: Open-Source Cavity Detection and Characterization on Molecular Dynamics Trajectories. Bioinformatics 2011, 27 (23), 3276–3285. [PubMed: 21967761]

(56). Liang J; Woodward C; Edelsbrunner H Anatomy of Protein Pockets and Cavities: Measurement of Binding Site Geometry and Implications for Ligand Design. Protein Sci. 1998, 7 (9), 1884–1897. [PubMed: 9761470]

(57). Eriksson AE; Baase WA; Zhang XJ; Heinz DW; Blaber M; Baldwin EP; Matthews BW Response of a Protein Structure to Cavity-Creating Mutations and Its Relation to the Hydrophobic Effect. Science 1992, 255 (5041), 178–183. [PubMed: 1553543]

(58). Björkman AJ; Mowbray SL Multiple Open Forms of Ribose-Binding Protein Trace the Path of its Conformational Change. J. Mol. Biol 1998, 279 (3), 651–664. [PubMed: 9641984]

(59). Taratula O; Hill PA; Khan NS; Carroll PJ; Dmochowski IJ Crystallographic Observation of 'Induced Fit' in a Cryptophane Host–Guest Model System. Nat. Commun 2010, 1 (1), 148. [PubMed: 21266998]

(60). Gunasekaran K; Ma B; Nussinov R Is Allostery an Intrinsic Property of All Dynamic Proteins? Proteins: Structure, Function, and Bioinformatics 2004, 57 (3), 433–443.

(61). Kuroki R; Weaver LH; Matthews BW A Covalent Enzyme-Substrate Intermediate with Saccharide Distortion in a Mutant T4 Lysozyme. Science 1993, 262 (5142), 2030–2033. [PubMed: 8266098]

(62). Maeno A; Sindhikara D; Hirata F; Otten R; Dahlquist Frederick W.; Yokoyama S; Akasaka K; Mulder Frans A. A.; Kitahara R Cavity as a Source of Conformational Fluctuation and High-Energy State: High-Pressure NMR Study of a Cavity-Enlarged Mutant of T4Lysozyme. Biophys. J 2015, 108 (1), 133–145. [PubMed: 25564860]

(63). Jamie; Victoria; Robert; Sida R; Rommie. Capturing Invisible Motions in the Transition from Ground to Rare Excited States of T4 Lysozyme L99A. Biophys. J 2016, 111 (8), 1631–1640. [PubMed: 27760351]

(64). Anand NN; Stephen ER; Narang SA Mutation of Active Site Residues in Synthetic T4-Lysozyme Gene and Their Effect on Lytic Activity. Biochem. Biophys. Res. Commun 1988, 153 (2), 862–868. [PubMed: 3382407]

(65). Shoichet BK; Baase WA; Kuroki R; Matthews BW A Relationship between Protein Stability and Protein Function. PNAS 1995, 92 (2), 452–456. [PubMed: 7831309]

(66). Hardy LW; Poteete AR Reexamination of the Role of Asp20 in Catalysis by Bacteriophage T4 Lysozyme. Biochemistry 1991, 30 (39), 9457–9463. [PubMed: 1892846]

(67). Kuroki R; Weaver LH; Matthews BW Structural Basis of the Conversion of T4 Lysozyme into a Transglycosidase by Reengineering the Active Site. PNAS 1999, 96 (16), 8949–8954. [PubMed: 10430876]

(68). Knoverek CR; Mallimadugula UL; Singh S; Rennella E; Frederick TE; Yuwen T; Raavicharla S; Kay LE; Bowman GR Opening of a Cryptic Pocket in β-lactamase Increases Penicillinase Activity. PNAS 2021, 118 (47), e2106473118. [PubMed: 34799442]

(69). Kuzmanic A; Bowman GR; Juarez-Jimenez J; Michel J; Gervasio FL Investigating Cryptic Binding Sites by Molecular Dynamics Simulations. Acc. Chem. Res 2020, 53 (3), 654–661. [PubMed: 32134250]

(70). Meller A; Lotthammer JM; Smith LG; Novak B; Lee LA; Kuhn CC; Greenberg L; Leinwand LA; Greenberg MJ; Bowman GR Drug Specificity and Affinity are Encoded in the Probability of Cryptic Pocket Opening in Myosin Motor Domains. Cold Spring Harbor Laboratory: 2022.

(71). Meller A; Bhakat S; Solieva S; Bowman GR Accelerating Cryptic Pocket Discovery using AlphaFold. Cold Spring Harbor Laboratory: 2022.

(72). Doukov TI; Blasiak LC; Seravalli J; Ragsdale SW; Drennan CL Xenon in and at the End of the Tunnel of Bifunctional Carbon Monoxide Dehydrogenase/Acetyl-CoA Synthase. Biochemistry 2008, 47 (11), 3474–3483. [PubMed: 18293927]
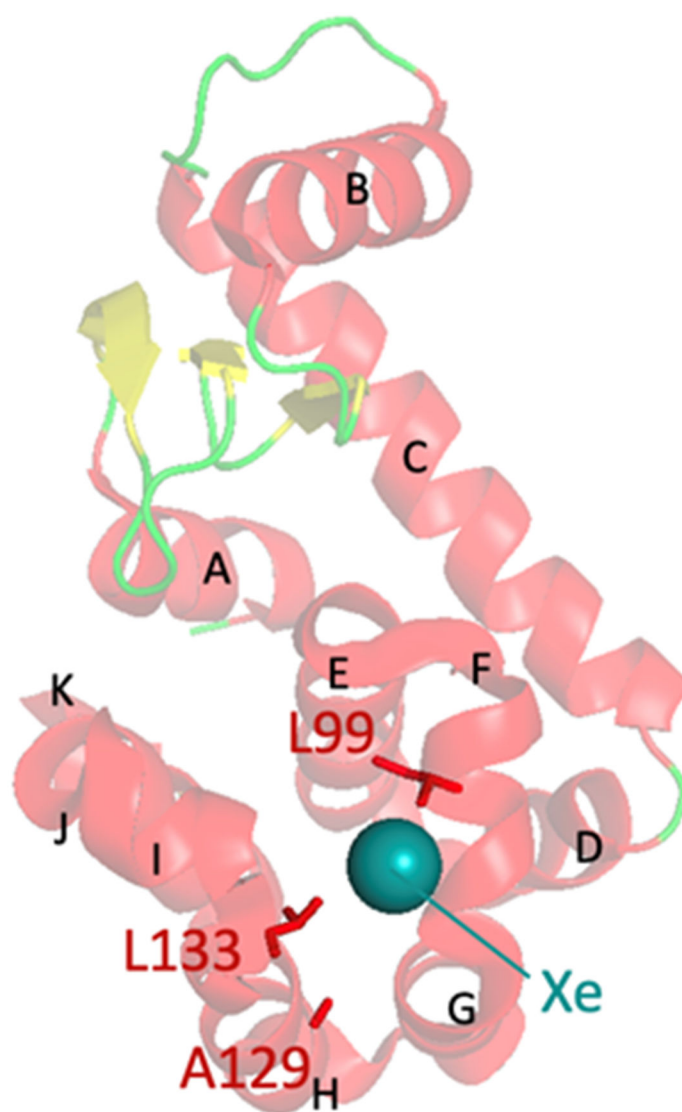
Figure 1.
Structural illustration of T4L(WT*) bound with Xe (blue sphere) (PDB: 1C6T). T4L is composed of five major α-helices (A, B, C, D - J, and K) (red), which contains 3_{10} helices in helices D to J, and three β-sheets (yellow) that are connected by free loops (green). Mutations at L99, L133, and A129 are indicated as sticks.
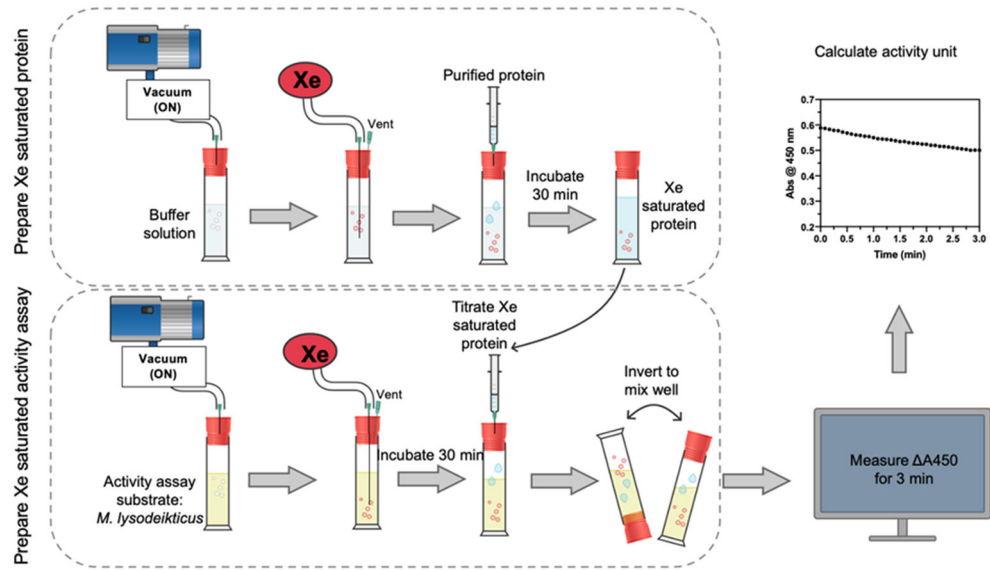
Figure 2.
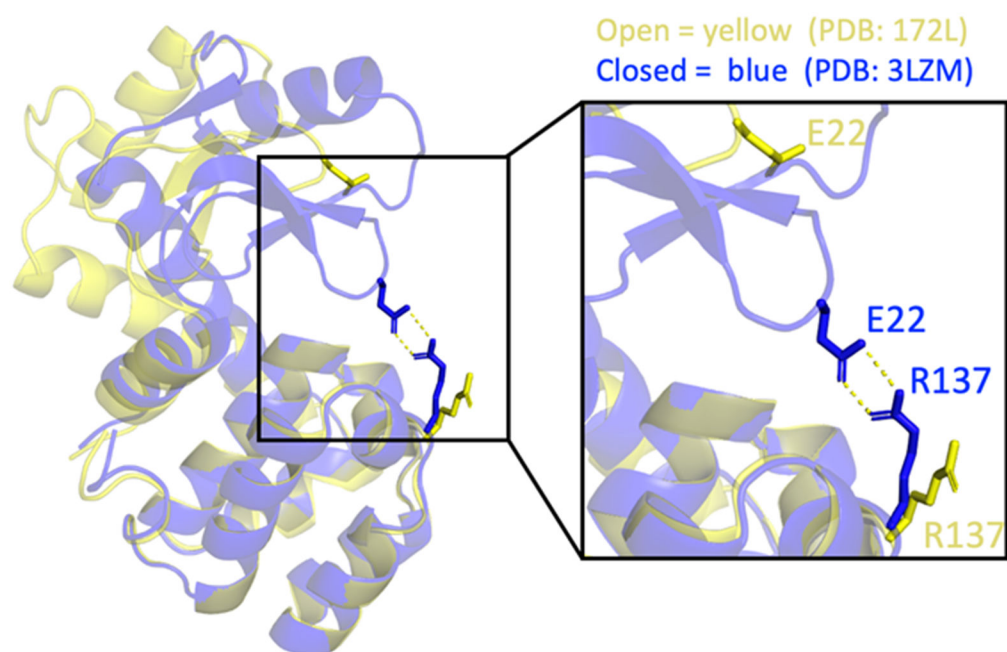Scheme of indirect gassing technique followed by lysozyme activity assay.

Figure 3.
Overlay of "open" (in yellow, PDB: 172L) and "closed" (in blue, PDB: 3LZM)
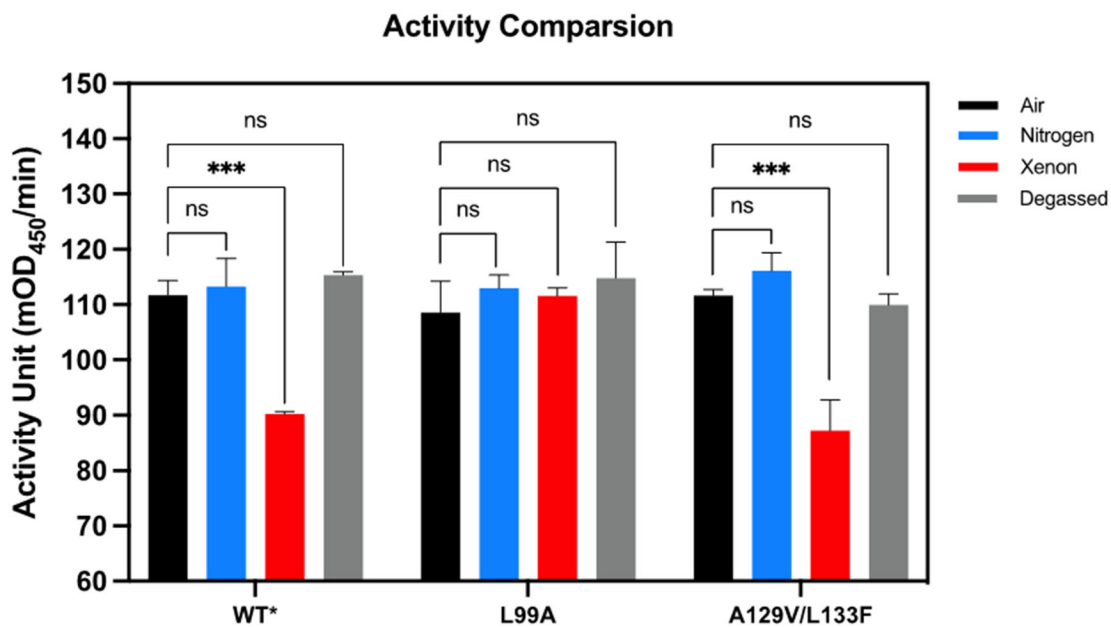conformations of T4L. The inter-domain salt bridge (E22-R137) is formed in the closed
conformation.

Figure 4.

Comparison of activities of different T4L enzymes at 7 μg/mL in saturated gas (air, nitrogen, or xenon) and degassed states. One-way ANOVA tests were performed to determine the significance of differences in activity measured in gassed/degassed states and in air. If p-value > 0.05, there is insignificant difference between the two groups (ns). If $0.01 < p < 0.05$, there is a significant difference (*). If $0.001 < p < 0.01$, there is a very significant difference (**). If $p < 0.001$, the difference is extremely significant (***).
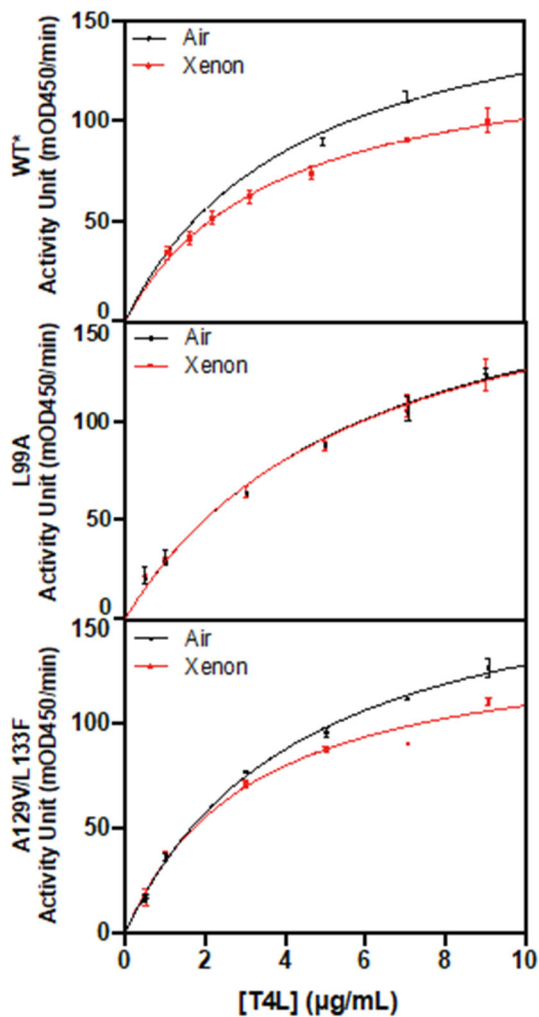
Figure 5.
Activity of T4L variants (top: WT*, middle: L99A, bottom: A129V/L133F) in various concentrations measured in air and saturated Xe solution. One activity unit is OD_{450} of 0.001 per minute at pH = 7.2 at 25 °C using a suspension of *Micrococcus lysodeikticus* as substrate in a 3.0 mL reaction volume.
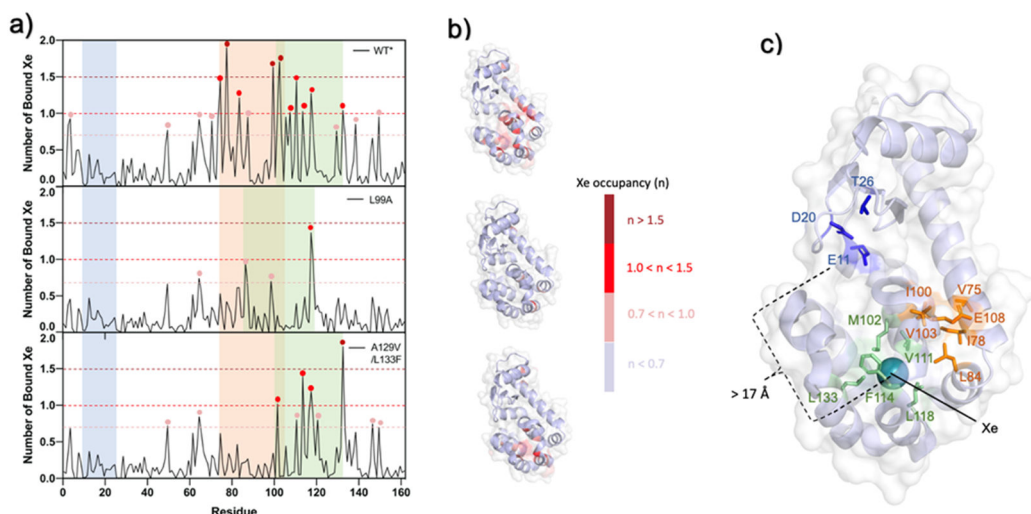
Figure 6.
(a) Average number of Xe atoms bound at the surface of WT* (top), L99A (middle), and A129V/L133F (bottom) in Xe flooding aMD simulations. Residues with more than 1.5 bound Xe atoms are highlighted in dark red, larger than 1.0 bound Xe in red, and larger than 0.7 bound Xe in light pink. Most of the residues that have highest Xe occupancy fall within the green region, corresponding to the primary Xe binding site. Other residues that have appreciable Xe occupancy are within the orange region, which corresponds to the cryptic binding site. Less than 0.05 Xe is bound to the active site residues (E11, D20, and T26) that are highlighted in the blue region. (b) Visualization of the Xe occupancy map on the T4L surface: WT* (top), L99A (middle), and A129V/L133F (bottom). (c) Visualization of Xe primary binding site, cryptic binding site, and active site on T4L. The distance between Xe binding site and the backbone of E11 in the active site is 17 Å.
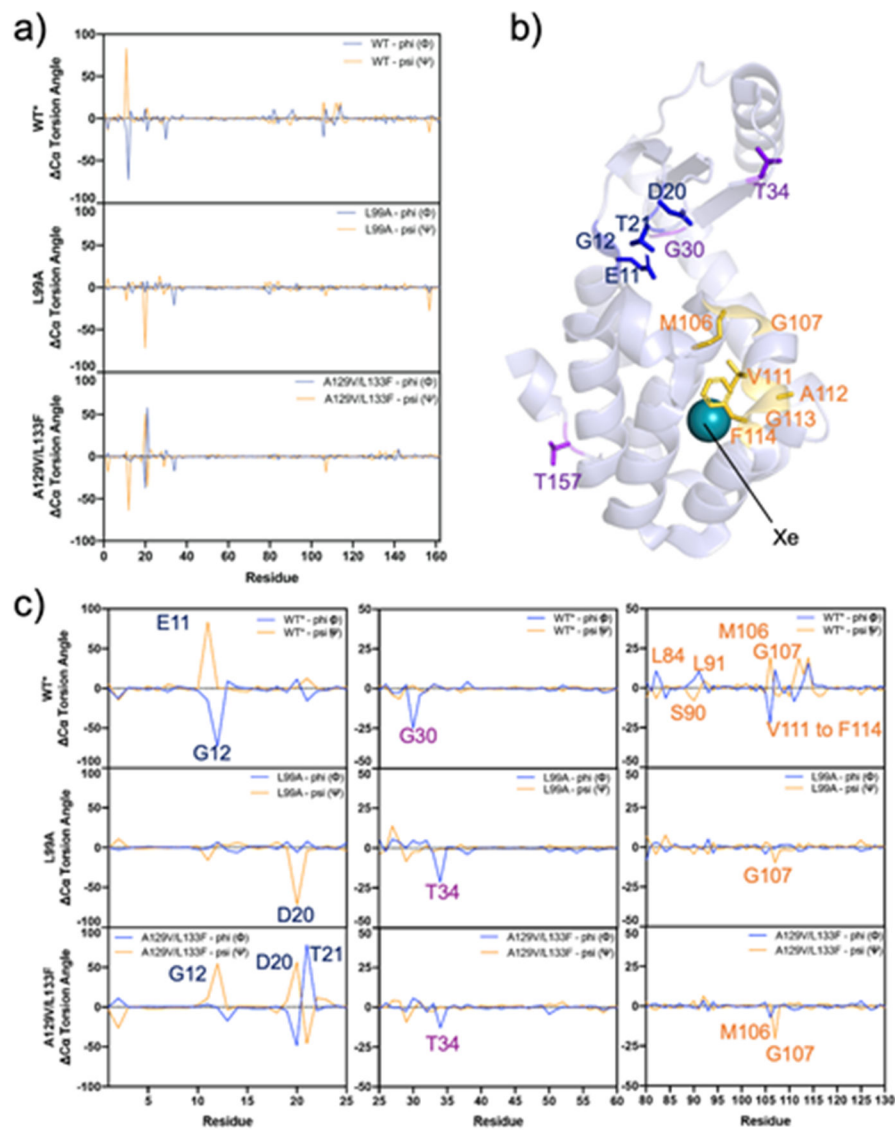
Figure 7.
(a) Cα-torsion angle difference plot for the whole protein for WT* (top), L99A (middle), and A129V/L133F (bottom) obtained by subtracting the angle for the Xe flooding simulation from that for the no-Xe simulation. (b) Structural illustration for Cα-torsion angle difference in WT*. (c) Zoomed-in Cα-torsion angle difference plot for WT* (top row), L99A (middle row), and A129V/L133F (bottom row).

Table 1.

Percentage of protein conformations that have detectable cavities, and the average cavity volumes (Å^3) calculated by MDpocket.

T4L variants	Simulation type	% conformations with detectable cavities	Average volume of detectable cavities (Å^3)
WT*	Xe-free	11.3%	85.9
	Xe flooding	92.9%	206.9
L99A	Xe-free	63.4%	139.8
	Xe flooding	96.4%	151.0
A129V/L133F	Xe-free	5.8%	88.1
	Xe flooding	70.8%	110.6

Table 2.

Percentage of protein in closed conformation in each of the T4L variants in the absence (Xe-free) and presence of Xe (Xe flooding). The closed conformation was estimated from the formation of the inter-domain salt bridge with a cut off at 3.6 Å.

T4L variants	Simulation type	% protein in closed conformation
WT*	Xe-free	33.4%
	Xe flooding	57.9%
L99A	Xe-free	63.6%
	Xe flooding	28.7%
A129V/L133F	Xe-free	67.4%
	Xe flooding	79.7%